Scaling analysis of anomalous Hall resistivity and magnetoresistance in the quasi-two-dimensional ferromagnet Fe_3GeTe_2

P. Saha, M. Singh, V. Nagpal, P. Das, and S. Patnaik*
School of Physical Sciences, Jawaharlal Nehru University, New Delhi 110067, India

(Received 29 September 2022; revised 14 December 2022; accepted 22 December 2022; published 11 January 2023)

Fe_3GeTe_2 is a two-dimensional van der Waals bonded layered compound that shows high-temperature itinerant ferromagnetism. We study aspects of the scattering mechanism in the single crystal of high-T_C Fe_3GeTe_2 via resistivity, magnetotransport, and Hall effect measurements. The quadratic temperature dependence of electrical resistivity below the T_C (210 K) points towards the dominance of electron-magnon scattering. A nonsaturating positive magnetoresistance (MR) is observed at low temperatures when the magnetic field is applied parallel to the sample plane. The linear negative MR at high fields for $T < T_C$ corroborates to the suppression in the magnon population due to the damping of spin waves. In the high-temperature regime ($T > T_C$), MR can be described by the scattering from spin fluctuations using the Khosla and Fischer model. Isothermal Hall resistivity curves unveil the presence of anomalous Hall resistivity. The correlation between magnetoresistance and side jump mechanism further reveals that the electron-magnon scattering is responsible for the side jump contribution to the anomalous Hall effect. Our results provide a clear understanding of the role of electron-magnon scattering on the temperature-driven evolution of the anomalous Hall effect that rules out its origin to be the topological band structure.

DOI: 10.1103/PhysRevB.107.035115

I. INTRODUCTION

Two-dimensional (2D) materials have attracted notable attention in the field of electronic devices due to their intriguing physical properties and the feasibility of fabricating complex structures out of them [1,2]. In recent years, extensive research on 2D materials have been carried out on van der Waals bonded heterostructures for their potential applications [3–5]. With the discovery of $Cr_2Ge_2Te_6$, which is a nearly ideal two-dimensional Heisenberg ferromagnet [6], the magnetism aspects have also come to the fore. In the recent past, Fe_3GeTe_2 (FGT), a 2D van der Waals material has gained significant interest due to its appealing properties such as uniaxial magnetocrystalline anisotropy [7], Kondo lattice behavior [8], large anomalous Hall current [9], and ionic gate tunable room temperature ferromagnetism [10]. Although the first report of the synthesis of FGT was published in 2006 [11], its high-temperature itinerant ferromagnetism (below 230 K) was reported recently [12]. Further, the magnetic force microscopy (MFM) measurements and density functional calculations have confirmed that this compound has an additional antiferromagnetic ground state below 152 K which is assigned to the oppositely aligned spin moments of Fe atoms between the adjacent layers [13]. It was therefore proposed to host two competing magnetic orderings between 152 and 214 K [13]. Previous reports have suggested that the ferromagnetic transition temperature T_C and the lattice parameters can be tuned by controlling the concentration of the Fe [14]. Hall effect measurements on FGT have revealed conventional anomalous behavior when the field is applied along the easy axis and it showed signatures of topological Hall effect when the field was applied along the *ab* plane due to the presence of a gauge field [15,16]. Magnetotransport properties of low $T_C \sim 138$ K phase of FGT have also been extensively studied [17]. Here, we report synthesis of FGT with a much higher $T_C \sim 210$ K. Our focus is to unravel the scattering mechanisms responsible for the magnetotransport behavior in FGT and its role in the temperature dependence of anomalous Hall effect (AHE). In the general theoretical framework, three different scattering mechanisms need to be taken into account to explain the origin of the anomalous Hall effect. One is the extrinsic skew scattering mechanism [18,19] which arises due to the intertwinement of scattering potentials and spin-orbit coupling. It has a linear dependence on longitudinal resistivity (ρ_{xx}). Second is the extrinsic side jump mechanism [20] which arises due to the transverse shift experienced by the charge carriers due to the scattering in the presence of spin-orbit interaction which leads to a quadratic dependence to longitudinal resistivity. Third, is the intrinsic Karplus-Luttinger (KL) mechanism [21] which results in an "anomalous velocity" originating from the Berry curvature of the occupied eigenstates and is related to the band structure of the respective material [9]. It also has a quadratic dependence to longitudinal resistivity. Nevertheless, the temperature-dependent change of AHE in FGT remains inconsistent and open to debate in both theoretical and experimental studies. The contribution to AHE due to KL mechanism is an inherent ground-state feature which is not supposed to change with temperature [21]. However, it has been demonstrated experimentally that the extrinsic side jump contribution to AHE can vary as a function of temperature [22]. Side jump

*spatnaik@jnu.ac.in

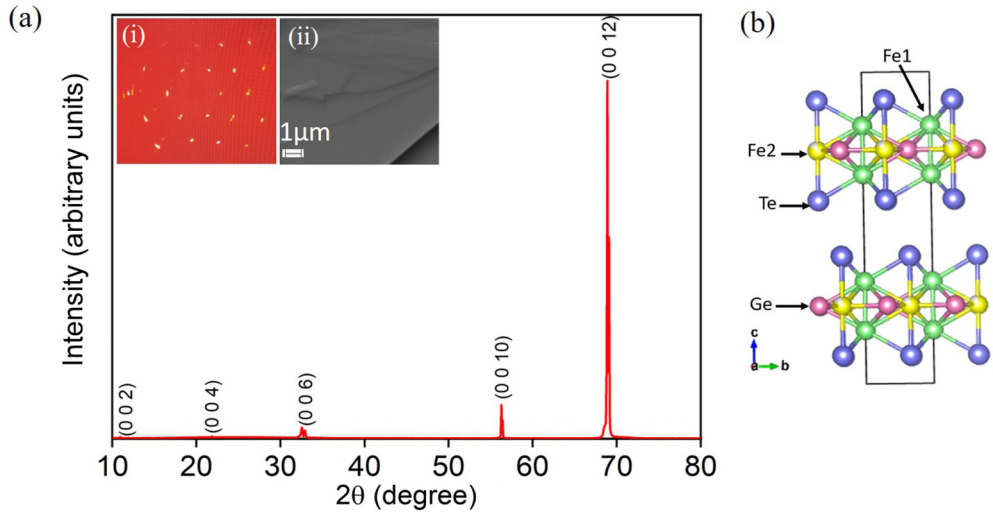

FIG. 1. (a) X-ray diffraction pattern of single-crystal FGT. Inset (i) shows the Laue diffraction pattern which confirms its single-crystalline nature. Inset (ii) is an SEM image depicting the layered morphology of FGT single crystal and the absence of any inhomogeneity. (b) Schematic view of the crystal structure of FGT.

contribution not only includes the coordinate shift of the wave packet [20] but also the scattering-induced contributions due to phonons and magnons [23]. Yang *et al.* have proposed that magnons tend to play a distinct role in the AHE as compared to phonons and other impurities [23]. Moreover, the electron-magnon scattering can control the temperature dependence of the side jump mechanism [24]. Being an itinerant ferromagnet with high T_C and a candidate of nodal line semimetal [9], FGT has been the best platform to study the interrelation between ferromagnetism and topology [9]. As reported, it exhibits a substantially large anomalous Hall current, which stems from the large Berry curvature associated with the nodal line [9]. However, the temperature dependence of AHE (and magnetoresistance) and its association with a specific scattering mechanism remain open to interpretation. In this paper, we discuss the microscopic origin of scattering mechanisms which affect the magnetoresistance property of FGT. Our results suggest that electron-magnon scattering plays a dominant role in the magnetoresistance (MR) and temperature dependence of anomalous Hall effect in Fe_3GeTe_2. This implies that the temperature-driven evolution of the magnetotransport behavior of van der Waals based topological materials can be explained through classical scattering mechanism without invoking its topological band structure.

II. EXPERIMENTAL TECHNIQUES

The single crystals of Fe_3GeTe_2 were synthesized by the chemical vapor transport method. Powders of iron (99.9%), germanium (99.999%), and tellurium (99.9%) were taken in the stoichiometric ratio and were ground for half an hour using a mortar and pestle. The homogeneous mixture was then cold pressed into pellets. These pellets were then inserted in a 30-cm-long quartz tube with iodine (2 mg/cm^3) as the transport agent. The tube was vacuum sealed and placed in a two-zone furnace with a temperature gradient of 750–700 °C for 1 wk. The plate-shaped crystals were deposited in the low-temperature zone of the tube. The crystal structure and phase at room temperature was identified using x-ray diffraction (XRD) in a Rigaku Miniflex 600 instrument. A Bruker x-ray diffractometer was used to perform the single-crystal XRD. The magnetotransport measurements were performed using a cryogenic built cryogen free magnet (8 T, 1.6 K). The temperature-dependent magnetization measurements were performed using the vibrating sample magnetometer attachment of a physical properties measurement system (PPMS). Scanning electron microscopy (SEM) was carried out using a Zeiss EVO40 SEM analyzer.

III. RESULTS AND DISCUSSIONS

A. X-ray diffraction

Figure 1(a) shows the XRD diffraction pattern of a single-crystal flake of FGT. The diffraction peaks dominantly correspond to the 00l planes and thus it depicts the single-crystalline nature of as-grown samples. Further, the Laue spots obtained using a single-crystal diffractometer [inset (i) of Fig. 1(a)] verify the single-crystalline nature of the sample and the lattice parameters are obtained as $a = b = 4.01$ Å and $c = 16.46$ Å, which is in good agreement with hexagonal crystal structure (space group $P6_3/mmc$) [11]. The SEM image of FGT crystal is shown in Fig. 1(a), inset(ii) that reflects the layered structure of the sample. The unit cell schematic of FGT is shown in Fig. 1(b). There are two inequivalent sites for Fe: Fe1 (green) forms a hexagonal arrangement with only Fe atoms and Fe2 (yellow) is covalently bonded to germanium in an adjacent layer. FGT has a structure in which the covalently bonded Fe_3Ge slabs are sandwiched by layers of tellurium atoms. Adjacent layers of tellurium atoms are bonded through van der Waals interaction.

B. Resistivity

Figure 2(a) shows the temperature-dependent resistivity (ρ) behavior of the FGT sample up to the room temperature.

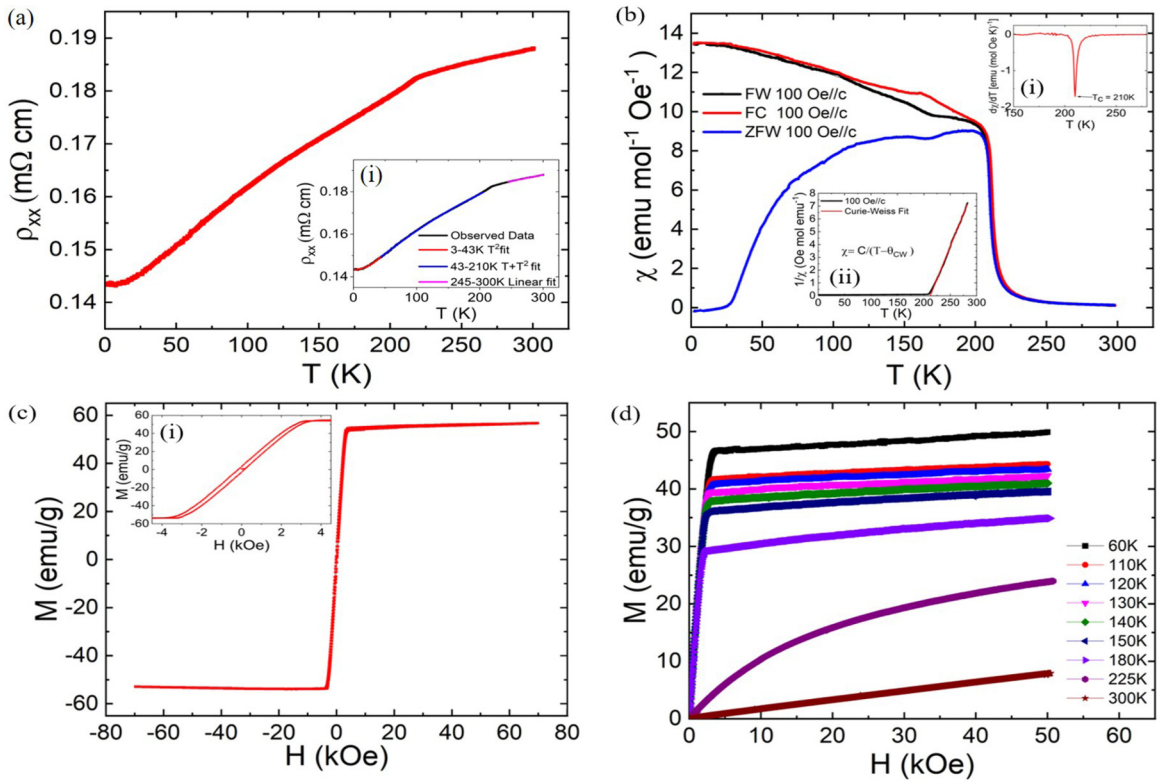

FIG. 2. (a) Temperature dependence of longitudinal resistivity. Inset (i) in (a) shows the theoretical fits for $\rho(T)$ for different temperature regimes. (b) is the temperature-dependent susceptibility for zero field cooled, field cooled, and field warming at $H = 100$ Oe. Inset (i) in (b) shows $d\chi/dT$ vs T behavior. Minima of the plot represent the Curie temperature at $T_C = 210$ K. Inset (ii) in (b) shows the temperature dependence of inverse susceptibility $1/\chi$ and its fitting using the Curie-Weiss equation. (c) shows the zoomed out view of the magnetization data at 2 K up to ± 7 T. Inset (i) of (c) shows the magnified view of field-dependent magnetization behavior at 2 K which shows a clear hysteresis. (d) Isothermal magnetization data at different temperatures up to 5 T for $H \parallel c$.

The resistivity increases with temperature implying the metallic nature. There is an abrupt change in the slope at 215 K which is reflective of the onset of a temperature-driven ferromagnetic phase transition. It is observed that residual resistivity (0.14 mΩ cm) is lower than earlier reports [9,15]. In general, the resistivity of a metallic sample is determined by several scattering mechanisms. In the following, ρ vs T behavior is studied in FGT in different temperature ranges and a corresponding microscopic mechanism has been identified. It is found that the temperature dependence of resistivity changes its nature in specific ranges: 3–43 K, 43–210 K, and 245–300 K. In the ferromagnetic state, electron-magnon scattering may contribute significantly. This is derived from the quadratic dependence of resistivity with temperature ($\rho \propto T^2$). The inset of Fig. 2(a) shows the observed data fitted with the theoretical curves for the different temperature ranges. In the low-temperature region ($3\ \text{K} < T < 43\ \text{K}$), the temperature-dependent resistivity shows a complete quadratic behavior ($\rho \propto T^2$) without any contribution from lower exponents. The behavior is ascribed to the electron-magnon scattering. As the temperature increases, that is, in the range $43\ \text{K} < T < 210\ \text{K}$, the resistivity data follows a sum of linear and quadratic dependence with temperature. This is evidence for admixture of electron-phonon scattering along with electron-magnon scattering. For temperatures above 245 K, which is a paramagnetic phase, a complete linear behavior has been obtained ($\rho \propto T$). This is ascribed to the dominance of the electron-phonon scattering mechanism.

C. Magnetization

The main panel of Fig. 2(b) shows the temperature-dependent magnetic susceptibility χ curve in the presence of magnetic field $H = 100$ Oe applied perpendicular to the ab plane of the sample under zero-field-cooled warming (ZFW), field-cooled cooling (FC), and field-cooled warming (FW) protocols. A steep growth in FW and ZFW susceptibility curves is seen at $T = 210$ K. This clearly marks the magnetic phase transition taking place in the compound. The Curie transition temperature is determined to be 210 K through the minimum in $d\chi/dT$ vs T curve [Fig. 2(b), inset (i)]. Just below the Curie temperature a notable splitting between FW, FC, and ZFW is observed. Similar behavior has been reported previously in FGT and has been attributed to the presence of irreversibility of ferromagnetic domains [11]. All three curves show a kink around 165 K which indicates the presence of a different magnetic phase identified as the competing ferromagnetic and antiferromagnetic phases [13]. However, some reports demonstrated that this dip in the three curves is due to the formation of Néel-type chiral spin spirals [25]. An additional kink is observed in ZFW data at 30 K, where the susceptibility drops to zero. This result confirms the

antiferromagnetic nature of the sample at lower temperatures and is consistent with the previous reports [13]. Figure 2(b), inset (ii) shows the temperature dependence of inverse magnetic susceptibility $1/\chi$. The paramagnetic region of the data ($T > 210$ K) obeys the Curie-Weiss law.

$$\chi = \frac{C}{T-\theta}, \tag{1}$$

where C is the Curie constant and θ is the Curie-Weiss temperature. The obtained values through this fit are $C = 9.84$ emu K/mol and $\theta = 212$ K. This positive value of Curie-Weiss temperature confirms the dominant ferromagnetic exchange interactions. The Curie constant is related to the number of unpaired electrons in the sample and the effective moment per magnetic ion is calculated to be 5.12 μ_B/Fe which is near to the theoretical value of 4.90 μ_B/Fe for the Fe^{2+} ion. Figure 2(c) shows the magnetic field dependent magnetization M-H curve at 2 K. Magnetization saturates to 50 emu/g at 0.36 T. This saturation depicts the ferromagnetic behavior and a clear hysteresis is observed in the inset of Fig. 2(c) with coercive field $H_C = 0.16$ T. Figure 2(d) shows the isothermal magnetization curves at different temperatures. The steep increment in magnetization followed by a saturation further depicts the robust ferromagnetic nature of FGT.

D. Magnetoresistance

The resistivity is customarily defined as a function of the relaxation time as defined below [26]:

$$\rho_{\text{total}} = a_1(\omega_c\tau)^n + a_2(1/\tau), \tag{2}$$

where τ is the electronic relaxation time and ω_c is the cyclotron frequency. The first term originates from the Lorentz force which restricts the motion of the free carriers. This constrained motion of the carriers raises the electrical resistivity with the increasing field and hence results in a positive MR. The second term is a sum of the contribution of the different scattering processes which tends to obstruct the conductivity and can be expressed as per Matthiessen's rule:

$$a_2(1/\tau) = \rho_{\text{res}} + \rho_{\text{e-e}}(T) + \rho_{\text{ph}}(T) + \rho_{\text{mag}}(T). \tag{3}$$

Here the first term ρ_{res} is due to the scattering due to impurities. Further, $\rho_{\text{e-e}}$, ρ_{ph}, and ρ_{mag} is due to electron-electron, electron-phonon, and electron-magnon scattering, respectively. The first three contributions (impurities, electrons, and phonons) are weakly dependent on an external magnetic field whereas the electron-magnon scattering is a field-dependent term. Magnons are the quasiparticles associated with the collective excitations in the spin-ordered ground state. At low temperatures, the probability of spin-flip transition reduces and so the population of magnons declines. Hence, the electron-magnon scattering is much enhanced at higher temperatures as compared to lower temperatures. However, the application of magnetic field tends to dampen these spin waves and this leads to suppression of the electron-magnon scattering. As a result, the longitudinal resistivity decreases with increasing magnetic field that results in a negative MR. A single crystal of dimension 1.7 mm × 1.2 mm × 0.46 mm was used for the magnetotransport measurements. Reports on electrical transport measurements on thin films of FGT have revealed the T_C to be similar to the bulk single crystal of FGT. Even the isothermal Hall measurements have shown the presence of anomalous Hall resistivity. Magnetotransport and magneto-optical Kerr effect measurements on Bi_2Te_3|FGT based heterostructure have revealed a sustained room temperature ferromagnetism up to 400 K. However, these results do not shed any light on the thickness-dependent behavior of magnetoresistance and on the scaling of anomalous Hall resistivity with longitudinal resistivity. In the absence of such studies, our results are specifically limited to an FGT single crystal of bulk thickness. Magnetotransport measurements on FGT crystal were performed with magnetic field applied perpendicular and parallel to the sample plane. In order to remove the contribution from Hall resistivity from the longitudinal MR the following equation was used:

$$\rho_{xx}(H,T) = \frac{\rho_{xx}(H,T) + \rho_{xx}(-H,T)}{2}. \tag{4}$$

Figures 3(a) and 3(b) show the isothermal MR with field applied parallel and perpendicular to the c axis. The MR is calculated using the following equation:

$$\frac{\Delta\rho_{xx}}{\rho_{xx}(T,0)} = \frac{\rho_{xx}(T,H) - \rho_{xx}(T,0)}{\rho_{xx}(T,0)}, \tag{5}$$

where $\rho_{xx}(T,0)$ and $\rho_{xx}(T,H)$ are the longitudinal resistivities at zero and nonzero field. For $H \parallel ab$, a positive MR at low temperature is observed. The sign of MR shifts from positive to negative at higher temperatures [Fig. 3(a)]. This crossover behavior of MR has not been observed in bulk FGT thus far. For $T > 10$ K under $H \parallel ab$ and for all temperatures in $H \parallel c$ a weak upturn in resistivity is observed which crosses into a negatively linear MR. This upturn in resistivity is obtained at fields for which the magnetization (M) is less than the saturated magnetization (M_s). This behavior is attributed to the scattering at domain walls which tend to enhance the resistivity. With the increasing field, M reaches M_s and the domain walls are annihilated after which only a negatively linear MR is observed. However, for higher temperature region ($T > T_C$) [Fig. 3(b)], in the paramagnetic phase of FGT, due to the absence of domain walls, there is a conspicuous change in the behavior of the curve. At low temperatures (for $H \parallel ab$), the positive MR indicates the dominance of the orbital MR [first term of Eq. (1) where $\rho_{xx} \propto (\omega_c\tau)^n$]. The field-dependent change in resistivity is given by

$$\frac{\Delta\rho_{xx}}{\rho_{xx}(0)} = (\mu\mu_0 H)^q, \tag{6}$$

where μ is the mobility and the exponent $q = 2$ according to standard theories [27]. However, experimental results have shown deviation from $q = 2$ where $1 < q < 2$ has been noted in many systems including ferromagnetic thin films [28,29] and doped semiconductors [30]. The inset of Fig. 3(b) shows the low-temperature MR at 3 K fitted using Eq. (6). The parameters obtained are $\mu = 0.0024$ m^2/V- s and $q = 1.34$ for 3 K and $\mu = 0.0016$ m^2/V s and $q = 1.27$ for 10 K. At moderate temperatures ($H \parallel ab$) and for $H \parallel c$, a linearly nonsaturating negative MR at high fields is observed. The negative MR% increases with increasing temperature. This behavior is a clear indication towards the dominance of the

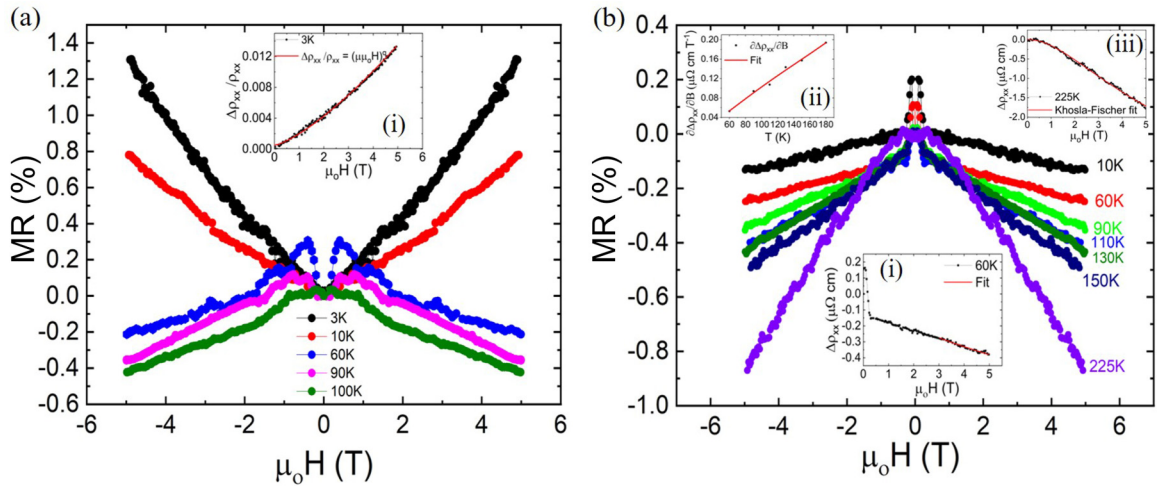

FIG. 3. (a) shows MR at different temperatures for $H \parallel ab$. Inset of (a) shows the field-dependent $\Delta\rho_{xx}/\rho_{xx}$ at 3 K and its corresponding fit using Eq. (6). (b) shows MR at different temperatures for $H \parallel c$. Inset (i) of (b) shows the field-dependent change in longitudinal resistivity $\Delta\rho_{xx}$ at 60 K and the red line is fit to Eq. (7). Inset (ii) of (b) shows the variation of $\partial\Delta\rho_{xx}/\partial B$ with temperature. The red line is the fit using Eq. (8). Inset (iii) of (b) shows the field-dependent behavior of $\Delta\rho_{xx}$ at 225 K with it's Khosla and Fischer fit [Eq. (9)] represented by the red line.

electron-magnon scattering in this temperature range and suppression of the same with evolving field. The amount of magnons is high at higher temperatures and the application of high field suppresses the amount of magnons and this results in larger negative MR at high temperatures. Raquet *et al.* [29] have provided an equation to describe the negative MR due to the electron-magnon scattering which is valid for fields below 100 T and for the temperature range of $T_C/5$ to $T_C/2$.

$$\Delta\rho_{xx}(T,B) \propto \frac{BT}{D(T)^2} \ln\frac{\mu_B B}{k_B T}, \tag{7}$$

where $D(T)$ is the magnon stiffness or the magnon mass renormalization, B is the magnetic field, and T is the temperature. The first-order approximation of magnon stiffness is described as $D(T) \sim D_0(1 - d_1T^2)$ where D_0 is the zero-temperature magnon mass and d_1 is a constant [29,31]. Inset (i) of Fig. 3(b) shows that the field-dependent longitudinal resistivity data fits well with the above equation and this confirms that the suppression in electron-magnon scattering is responsible for the linearly negative MR. Furthermore, the slope of the high-field MR showed a significant dependence with temperature and is described by the following equation [29]:

$$\frac{\partial\Delta\rho_{xx}}{\partial B} \propto T(1 + 2d_1T^2)[\ln(T) + c_{te}], \tag{8}$$

where d_1 is a constant which depends on the zero-temperature magnon mass and c_{te} is a temperature-independent term. d_1 is of the order of 10^{-6} K^{-2} for Fe, Co, and Ni thin films [29]. The temperature-dependent variation of the high-field resistivity slope is shown in inset (ii) of Fig. 3(b). The above equation provides a good fit for the data with $d_1 = 10^{-5}$ K^{-2}. The large value of d_1 depicts a stronger dependence of magnon stiffness on temperature. For $T > T_C$, an enhancement in the negative MR% is observed. This arises due to the scattering of conduction electrons from the fluctuating local moments. In this regime, a negative nonlinear MR is observed which is unlike the linear MR for $T < T_C$. Khosla and Fischer [30] have proposed a model to study the scattering from In impurities in CdS and have subsequently predicted this kind of MR. It is described by the following equation:

$$\Delta\rho_{xx} = -b_1 \ln[1 + (b_2\mu_0 H)^2], \tag{9}$$

where b_1 and b_2 are constants. For $T > T_C$, spin fluctuations become predominant and the MR is best described by the semiempirical formula of Khosla and Fischer as shown in inset (iii) of Fig. 3(b). The parameters returned from this fit are $b_1 = 1.08$ μΩ cm and $b_2 = 0.39$ m^2/V s. It is noteworthy that the Khosla-Fischer formula does not fit for the isothermal field-dependent resistivity in the range $T < T_C$ and this marks towards the magnetic phase transition and independently confirms that different scattering processes are involved in these two regimes.

E. Anomalous Hall effect

In ferromagnets, the magnetic field-driven evolution of the transverse resistivity ρ_{xy} is known as the anomalous Hall resistivity (ρ_{xy}^{ah}). It is described by the following equation:

$$\rho_{xy} = \rho_{xy}^{oh} + \rho_{xy}^{ah} = R_o\mu_o H + 4\pi R_s M_s, \tag{10}$$

where R_o and R_s are the ordinary and anomalous Hall coefficients, respectively. M_s is the saturation magnetization obtained from the isothermal magnetization curves as shown in Fig. 2(d). The first term is called the ordinary Hall resistivity which arises due to the deflection of charge carriers as a consequence of the Lorentz force acting on them. The second term is the anomalous Hall resistivity. Due to this additional term, the total Hall resistivity experiences a sharp rise with the evolving field followed by a saturation, much like the field-dependent magnetization behavior. Hall resistivity is the transverse resistivity measured at constant temperature with evolving magnetic field as shown in Fig. 4(a). For temperatures below T_C, there is a steep rise in the Hall resistivity up to

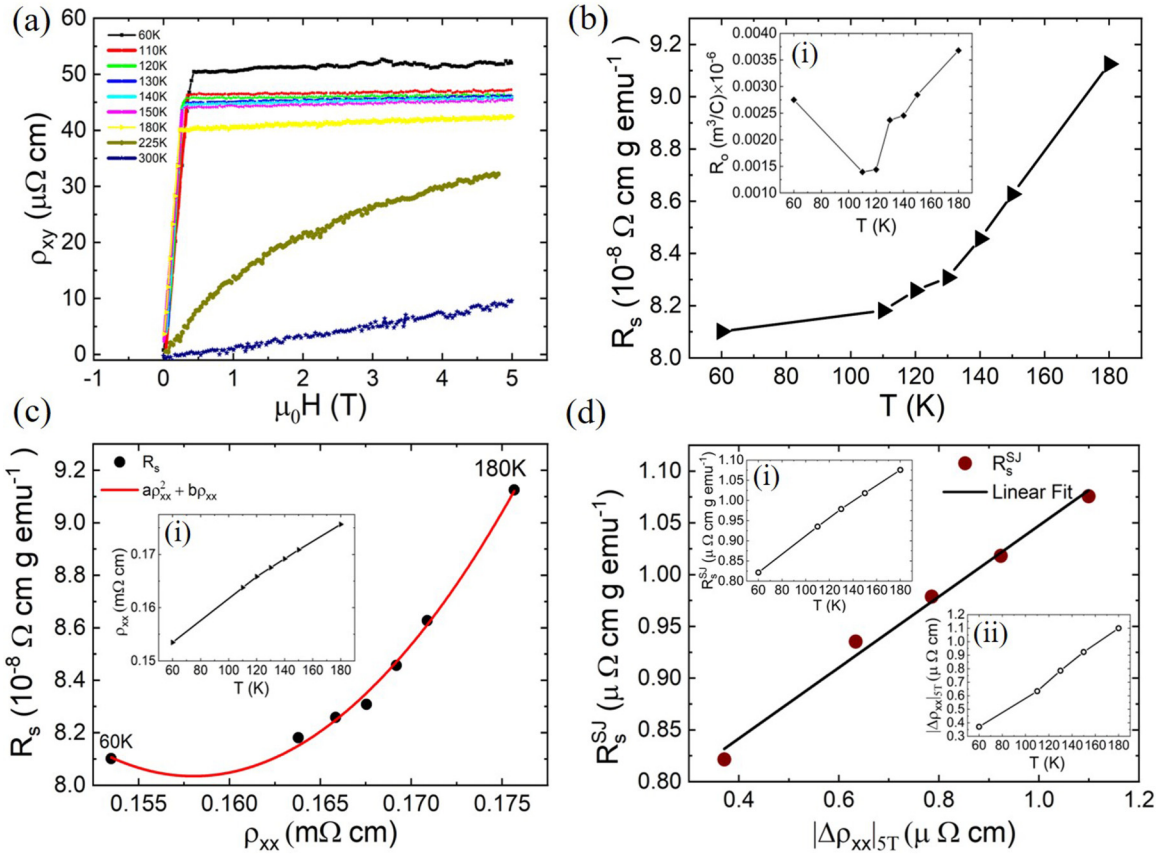

FIG. 4. (a) Isothermal Hall resistivity curves as a function of magnetic field at distinct temperatures. (b) Temperature dependence of anomalous Hall coefficient R_s determined using Eq. (11). Inset of (b) shows the variation of normal Hall coefficient R_o with temperature. (c) Scaling of R_s vs ρ_{xx} according to Eq. (12). Inset of (c) shows variation of ρ_{xx} with temperature. (d) shows linear fit between side jump contribution to anomalous Hall coefficient, R_{sj}, and change in resistivity with field ($|\Delta\rho_{xx}|_{5T}$). Insets (i) and (ii) show the variation of R_{sj} and ($|\Delta\rho_{xx}|_{5T}$) as a function of temperature.

a particular field after which it almost reaches saturation. This is a clear indication of the presence of a nonzero anomalous Hall response in our sample. When field was applied along the *ab* plane, the Hall resistivity shows a cusplike irregularity. This is due to the gauge field which stems from the noncoplanar spin configuration and is congruent with the previous reports [15,16]. The normal Hall coefficient R_o can be determined by the slope of the Hall resistivity data in the high-field region. The sign of this slope determines the type of charge carriers involved. Inset (i) of Fig. 4(b) shows that R_o tends to increase with temperature. Its positive sign at all temperatures indicates that the majority of charge carriers are holes. The anomalous Hall resistivity ρ_{xy}^{ah} is obtained by extrapolating the Hall resistivity data from the high field to the y axis. The anomalous Hall coefficient is determined using the following relation:

$$R_s = \frac{\rho_{xy}^{ah}}{4\pi M_S}. \tag{11}$$

Figure 4(b) shows that R_s increases considerably with temperature. It is approximately three orders of magnitude larger than R_o. This shows the strong dominance of the anomalous Hall resistivity over the total Hall resistivity. Lorentz force deflection cannot interpret this large R_s. In ferromagnets the R_s is a function of longitudinal resistivity ρ_{xx} specified by the following relation:

$$R_s = a\rho_{xx}^2 + b\rho_{xx}. \tag{12}$$

Here, a denotes the strength of the side jump contribution [20] as well as the intrinsic Berry phase contribution [21] and b corresponds to the strength of the skew scattering contribution [18,19]. In order to determine the dominant scattering contribution, $R_s(T)$ has been scaled with ρ_{xx} using Eq. (12) as shown in Fig. 4(c). The parameters returned from the fit are $a = 34.86\ \mathrm{g\,emu^{-1}\,\Omega^{-1}\,cm^{-1}}$ and $b = -0.011\ \mathrm{g\,emu^{-1}}$. The inset of Fig. 4(c) shows the temperature-dependent change of ρ_{xx}. It is evident from the parameters that the intrinsic Berry phase and/or side jump contribution ($R_s^{sj,i}$) dominates the anomalous Hall effect. This result is in agreement with the earlier reports [9,15]. However, separating the extrinsic side jump (R_s^{sj}) and intrinsic Berry phase related contribution (R_s^{i}) is a challenge, since both of them show quadratic dependence to longitudinal resistivity ($\propto \rho_{xx}^2$). The negative sign of the skew scattering contribution b, indicates that it is acting in the opposite direction as compared to $R_s^{sj,i}$. The intrinsic contribution to AHE in FGT has been previously linked to its topological nodal line band structure [9]. Moreover, this intrinsic contribution is an inherent property of a system and is weakly dependent on temperature even though ρ_{xx} varies

with temperature [32,33]. It has already been demonstrated that the electron-magnon scattering can affect the side jump scattering [24]. In FGT, both the temperature-dependent resistivity and MR measurement results have shown the dominance of the electron-magnon scattering. In order to confirm the role of magnons and its effect on the temperature dependence of the side jump mechanism, the temperature dependence change in resistivity under field $|\Delta\rho_{xx}|_{5T}$ is plotted with R_s^{sj}. Insets (i) and (ii) of Fig. 4(d) show the change in R_s^{sj} and $|\Delta\rho_{xx}|_{5T}$ with temperature. It is evident from the linear fit of the data in Fig. 4(d) that the temperature dependence of R_s^{sj} stems from the electron-magnon scattering. Our results clearly suggest that, despite the dominance of the intrinsic contribution to AHE [9,15] and its connection to the topological band structure [9], the temperature dependence of AHE can be explained by the electron-magnon scattering mechanism.

IV. CONCLUSION

In summary, the analysis of temperature-dependent resistivity and magnetoresistance have revealed the dominant scattering mechanisms in single crystals of Fe_3GeTe_2. The change in resistivity as a function of temperature in the ferromagnetic phase of Fe_3GeTe_2 is dominated by the electron-magnon scattering. At low temperatures, with the field applied parallel to the sample plane, a nonsaturating positive magnetoresistance is obtained. This indicates dominance of Lorentz force on the charge carriers. At moderate temperatures, both in cases of field applied parallel and perpendicular to the sample plane, the negative magnetoresistance is described by the reduction in electron-magnon scattering. This effect weakens as the temperature is decreased. The linearity of the magnetoresistance in the high-field region further confirms the dominance of the electron-magnon scattering. The large magnetoresistance in the paramagnetic phase is explained by the scattering from spin fluctuations. Below T_C, the anomalous Hall coefficient scales with the longitudinal resistivity that reveals that it is driven by the combination of Berry phase and extrinsic side jump mechanisms. On the other hand, temperature-dependent magnetoresistance at high field is correlated with the side jump contribution only. This validates that the side jump contribution originates from the electron-magnon scattering. In essence, the temperature dependence of anomalous Hall effect in Fe_3GeTe_2 is adequately explained by the classical scattering mechanisms without the need to invoke its topological band structure.

ACKNOWLEDGMENTS

P.S., V.N., and P.D. acknowledge UGC-NET JRF for financial support. M.S. thanks CSIR for providing JRF. We are grateful to the FIST program of the Department of Science and Technology, Government of India for the use of the low-temperature high magnetic field measurement facility at JNU. We acknowledge Advanced Instrumentation Research Facility (AIRF), JNU for use of the PPMS measurement facility.

[1] A. H. Castro Neto, F. Guinea, N. M. R. Peres, K. S. Novoselov, and A. K. Geim, The electronic properties of graphene, Rev. Mod. Phys. **81**, 109 (2009).

[2] Y. Zhu, S. Murali, W. Cai, X. Li, J. W. Suk, J. R. Potts, and R. S. Ruoff, Graphene and graphene oxide: Synthesis, properties, and applications, Adv. Mater. **22**, 3906 (2010).

[3] M. Chhowalla, H. S. Shin, G. Eda, L.-J. Li, K. P. Loh, and H. Zhang, The chemistry of two-dimensional layered transition metal dichalcogenide nanosheets, Nat. Chem. **5**, 263 (2013).

[4] G. R. Bhimanapati, Z. Lin, V. Meunier, Y. Jung, J. Cha, S. Das, D. Xiao, Y. Son, M. S. Strano, V. R. Cooper *et al.*, Recent advances in two-dimensional materials beyond graphen, ACS Nano **9**, 11509 (2015).

[5] S. Z. Butler, S. M. Hollen, L. Cao, Y. Cui, J. A. Gupta, H. R. Gutiérrez, T. F. Heinz, S. S. Hong, J. Huang, A. F. Ismach *et al.*, Progress, challenges, and opportunities in two-dimensional materials beyond graphene, ACS Nano **7**, 2898 (2013).

[6] C. Gong, L. Li, Z. Li, H. Ji, A. Stern, Y. Xia, T. Cao, W. Bao, C. Wang, Y. Wang *et al.*, Discovery of intrinsic ferromagnetism in two-dimensional van der Waals crystals, Nature (London) **546**, 265 (2017).

[7] N. León-Brito, E. D. Bauer, F. Ronning, J. D. Thompson, and R. Movshovich, Magnetic microstructure and magnetic properties of uniaxial itinerant ferromagnet Fe_3GeTe_2, J. Appl. Phys. **120**, 083903 (2016).

[8] Y. Zhang, H. Lu, X. Zhu, S. Tan, W. Feng, Q. Liu, W. Zhang, Q. Chen, Y. Liu, and X. Luo *et al.*, Emergence of Kondo lattice behavior in a van der Waals itinerant ferromagnet, Fe_3GeTe_2, Sci. Adv. **4**, eaao6791 (2018).

[9] K. Kim, J. Seo, E. Lee, K.-T. Ko, B. Kim, B. G. Jang, J. M. Ok, J. Lee, Y. J. Jo, W. Kang *et al.*, Large anomalous Hall current induced by topological nodal lines in a ferromagnetic van der Waals semimetal, Nat. Mater. **17**, 794 (2018).

[10] Y. Deng, Y. Yu, Y. Song, J. Zhang, N. Z. Wang, Z. Sun, Y. Yi, Y. Z. Wu, S. Wu, J. Zhu *et al.*, Gate-tunable room-temperature ferromagnetism in two-dimensional Fe_3GeTe_2, Nature (London) **563**, 94 (2018).

[11] H.-J. Deiseroth, K. Aleksandrov, C. Reiner, L. Kienle, and R. K. Kremer, Fe_3GeTe_2 and Ni_3GeTe_2—Two new layered transition-metal compounds: Crystal structures, HRTEM investigations, and magnetic and electrical properties, Eur. J. Inorg. Chem. **2006**, 1561 (2006).

[12] B. Chen, J. Yang, H. Wang, M. Imai, H. Ohta, C. Michioka, K. Yoshimura, and M. Fang, Magnetic properties of layered itinerant electron ferromagnet Fe_3GeTe_2, J. Phys. Soc. Jpn. **82**, 124711 (2013).

[13] J. Yi, H. Zhuang, Q. Zou, Z. Wu, G. Cao, S. Tang, S. Calder, P. Kent, D. Mandrus, and Z. Gai, Competing antiferromagnetism in a quasi-2D itinerant ferromagnet: Fe_3GeTe_2, 2D Mater. **4**, 011005 (2016).

[14] A. F. May, S. Calder, C. Cantoni, H. Cao, and M. A. McGuire, Magnetic structure and phase stability of the van der Waals bonded ferromagnet $Fe_{3-x}GeTe_2$, Phys. Rev. B **93**, 014411 (2016).

[15] Y. Wang, C. Xian, J. Wang, B. Liu, L. Ling, L. Zhang, L. Cao, Z. Qu, and Y. Xiong, Anisotropic anomalous Hall effect in triangular itinerant ferromagnet Fe_3GeTe_2, Phys. Rev. B **96**, 134428 (2017).

[16] R. R. Chowdhury, S. DuttaGupta, C. Patra, O. A. Tretiakov, S. Sharma, S. Fukami, H. Ohno, and R. P. Singh, Unconventional Hall effect and its variation with co-doping in van der Waals Fe_3GeTe_2, Sci. Rep. **11**, 14121 (2021).

[17] J. Ke, M. Yang, W. Xia, H. Zhu, C. Liu, R. Chen, C. Dong, W. Liu, M. Shi, Y. Guo *et al.*, Magnetic and magneto-transport studies of two-dimensional ferromagnetic compound Fe_3GeTe_2, J. Phys.: Condens. Matter **32**, 405805 (2020).

[18] J. Smit, The spontaneous Hall effect in ferromagnetics I, Physica **21**, 877 (1955).

[19] J. Smit, The spontaneous Hall effect in ferromagnetics II, Physica **24**, 39 (1958).

[20] L. Berger, Side-jump mechanism for the Hall effect of ferromagnets, Phys. Rev. B **2**, 4559 (1970).

[21] R. Karplus and J. Luttinger, Hall Effect in Ferromagnetics, Phys. Rev. **95**, 1154 (1954).

[22] Y. Tian, L. Ye, and X. Jin, Proper Scaling of the Anomalous Hall Effect, Phys. Rev. Lett. **103**, 087206 (2009).

[23] S. A. Yang, H. Pan, Y. Yao, and Q. Niu, Scattering universality classes of side jump in the anomalous Hall effect, Phys. Rev. B **83**, 125122 (2011).

[24] R. P. Jena, D. Kumar, and A. Lakhani, Scaling analysis of anomalous Hall resistivity in the Co_2TiAl Heusler alloy, J. Phys.: Condens. Matter **32**, 365703 (2020).

[25] H. Wang, C. Wang, Z.-A. Li, H. Tian, Y. Shi, H. Yang, and J. Li, Characteristics and temperature-field-thickness evolutions of magnetic domain structures in van der Waals magnet Fe_3GeTe_2 nanolayers, Appl. Phys. Lett. **116**, 192403 (2020).

[26] G. Taylor, A. Isin, and R. Coleman, Resistivity of iron as a function of temperature and magnetization, Phys. Rev. **165**, 621 (1968).

[27] A. B. Pippard, *Magnetoresistance in Metals* (Cambridge University Press, Cambridge, UK, 1989), Vol. 2.

[28] N. A. Porter, J. C. Gartside, and C. H. Marrows, Scattering mechanisms in textured FeGe thin films: Magnetoresistance and the anomalous Hall effect, Phys. Rev. B **90**, 024403 (2014).

[29] B. Raquet, M. Viret, E. Sondergard, O. Cespedes, and R. Mamy, Electron-magnon scattering and magnetic resistivity in 3*d* ferromagnets, Phys. Rev. B **66**, 024433 (2002).

[30] R. Khosla and J. Fischer, Magnetoresistance in degenerate CdS: Localized magnetic moment, Phys. Rev. B **2**, 4084 (1970).

[31] A. P. Mihai, J. P. Attané, A. Marty, P. Warin, and Y. Samson, Electron-magnon diffusion and magnetization reversal detection in FePt thin films, Phys. Rev. B **77**, 060401(R) (2008).

[32] N. Nagaosa, J. Sinova, S. Onoda, A. H. MacDonald, and N. P. Ong, Anomalous Hall effect, Rev. Mod. Phys. **82**, 1539 (2010).

[33] T. Miyasato, N. Abe, T. Fujii, A. Asamitsu, S. Onoda, Y. Onose, N. Nagaosa, and Y. Tokura, Crossover Behavior of the Anomalous Hall Effect and Anomalous Nernst Effect in Itinerant Ferromagnets, Phys. Rev. Lett. **99**, 086602 (2007).